Supplementary Material

A facile neoteric technique to achieve [SrF_2:Eu^{3+}@SiO_2]//[SrF_2:Tb^{3+}@SiO_2] Janus yolk-shell nanofibers with ideal white-light emission via triple-inhibiting energy transfer between Tb^{3+} and Eu^{3+} ions

Ning Li[1, 2], Hong Shao[1]*, Xiaohan Liu[1], Haina Qi[2], Dan Li[1], Wensheng Yu[1], Guixia Liu[1], Xiangting Dong[1, 2]*, Xuejian Zhang[2]*

1. Key Laboratory of Applied Chemistry and Nanotechnology at Universities of Jilin Province, Changchun University of Science and Technology, Changchun 130022, China

2. School of Materials Science and Engineering, Jilin Jianzhu University, Changchun, 130018, China

*E-mail: shaoh169@cust.edu.cn; xtdong@cust.edu.cn; zxj_0620@163.com Fax: (+86) 431-85383815; Tel.: (+86) 431-85582575

Chemicals reagents and characterization techniques

Strontium acetate [$Sr(CH_3COO)_2$, AR], europium oxide (Eu_2O_3, 99.99%), terbium oxide (Tb_4O_7, 99.99%) and polyvinylpyrrolidone (PVP, K90, M.W.=1,300,000) were purchased from Aladdin Reagent Co., Ltd. *N, N*-dimethylformamide (DMF, AR), tetraethyl orthosilicate (TEOS, AR) and ammonium hydrogen difluoride (NH_4HF_2, AR) were purchased from Sinopharm Chemical Reagent Co., Ltd. Activated carbon granules were bought from Tianjin Guangfu Technology Development Co., Ltd. Concentrated nitric acid (HNO_3, AR) was purchased from Beijing Chemical Works. Deionized water was homemade. All chemicals were directly used as received without further purification.

X-ray diffraction (XRD) data were collected on an X-ray diffractometer made by Bruker Corporation with the model of Ultima IV, and Cu Kα radiation was used. The morphology of the samples was observed by a JSM-7610F field emission scanning electron microscope (FESEM) made by JEOL Company and a Tecnai G2 20S-Twin transmission electron microscope (TEM). The elemental analysis of the specimens was performed by an energy-dispersive spectroscopy (EDS, X-MaxN80) attached to the FESEM. A Hitachi fluorescence spectrophotometer (F-7000) was utilized to accomplish the luminescent analysis of the samples.

Table S1 Compositions of the spinning liquid I

Sample	Spinning liquid I					
	$Sr(CH_3COO)_2$/g	Eu_2O_3/g	DMF/g	Deionized water/g	TEOS/g	PVP/g
SrF_2:9%Eu^{3+}@SiO_2	1.3175	0.1114	2.0000	4.4000	0.8000	1.2000

Table S2 Compositions of the spinning liquid II

Samples	Spinning liquid II					
	$Sr(CH_3COO)_2$/g	Tb_4O_7/g	DMF/g	Deionized water/g	TEOS/g	PVP/g
SrF_2:1%Tb^{3+}@SiO_2	1.5653	0.0144	2.0000	4.4000	0.8000	1.2000
SrF_2:3%Tb^{3+}@SiO_2	1.4979	0.0421	2.0000	4.4000	0.8000	1.2000
SrF_2:5%Tb^{3+}@SiO_2	1.4338	0.0686	2.0000	4.4000	0.8000	1.2000
SrF_2:7%Tb^{3+}@SiO_2	1.3725	0.0939	2.0000	4.4000	0.8000	1.2000
SrF_2:9%Tb^{3+}@SiO_2	1.3137	0.1181	2.0000	4.4000	0.8000	1.2000

Table S3 Compositions of the spinning liquids for preparing specimens used for verifying energy transfer between Eu^{3+} and Tb^{3+}

Specimens	Spinning liquids					
	$Sr(CH_3COO)_2$/g	Eu_2O_3/g	Tb_4O_7/g	DMF/g	deionized water/g	PVP/g
SrF_2:9%Eu^{3+} nanofibers	1.3175	0.1114	0	2.0000	5.2000	1.2000
SrF_2:7%Tb^{3+} nanofibers	1.3725	0	0.0939	2.0000	5.2000	1.2000
SrF_2:9%Eu^{3+}, 7%Tb^{3+} nanofibers	1.1299	0.1034	0.0856	2.0000	5.2000	1.2000

Figure S1 Physical image of the di-axis parallel spinneret

Results and discussion

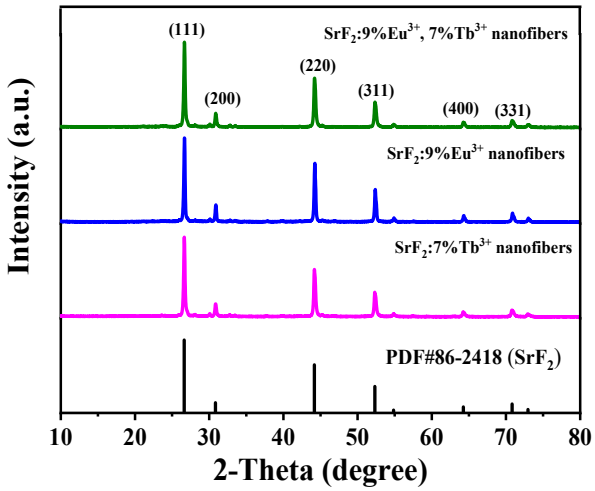

Figure S2 XRD patterns of SrF_2:9%Eu^{3+} nanofibers, SrF_2:7%Tb^{3+} nanofibers and SrF_2:9%Eu^{3+}, 7%Tb^{3+} nanofibers with PDF standard card of SrF_2

The XRD patterns of SrF_2:9%Eu^{3+} nanofibers, SrF_2:7%Tb^{3+} nanofibers and SrF_2:9%Eu^{3+}, 7%Tb^{3+} nanofibers are provided in Figure S2, and it can be seen from the figure that all diffraction peaks are consistent with the standard card of SrF_2 (PDF#86-2418), meaning that pure-phase SrF_2 doped with rare earth ions specimens are obtained.

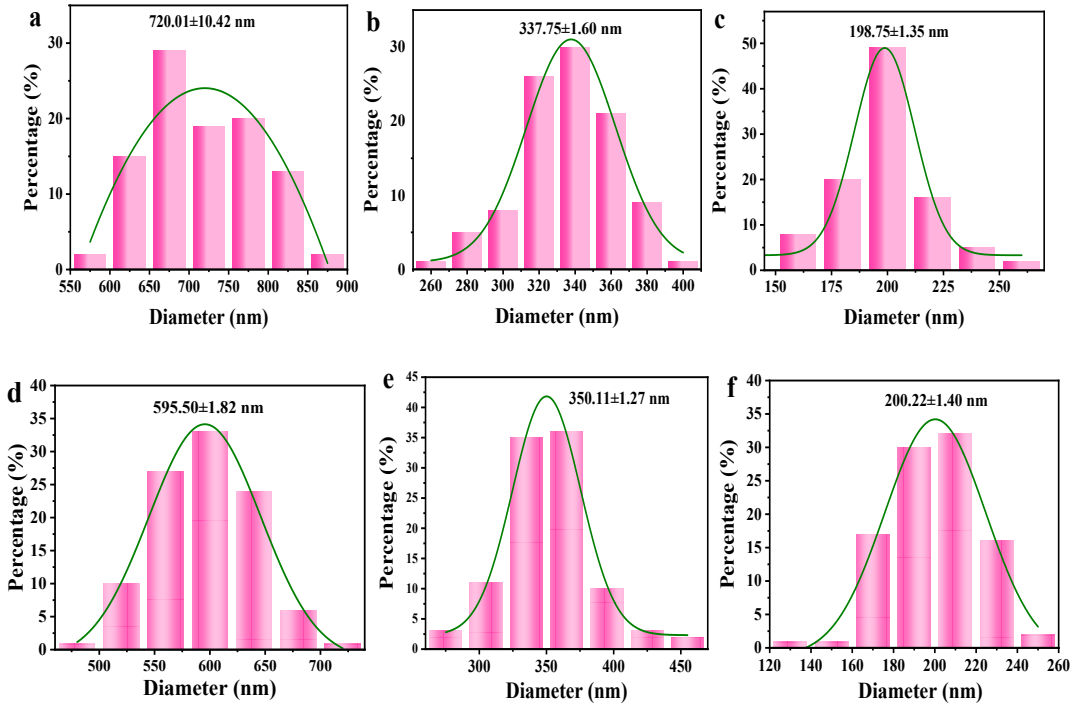

Figure S3 Histograms of diameters distribution of {PVP/[$Sr(CH_3COO)_2$+$Eu(NO_3)_3$+TEOS]}//{PVP/[$Sr(CH_3COO)_2$+$Tb(NO_3)_3$+TEOS]} JCNFs (a), shell (b) and yolk (c) of each side for [SrF_2:9%Eu^{3+}@SiO_2]//[SrF_2:7%Tb^{3+}@SiO_2] JYSNFs; Histograms of diameters distribution of PVP/[$Sr(CH_3COO)_2$+$Eu(NO_3)_3$+$Tb(NO_3)_3$+TEOS] CNFs (d), shell (e) and yolk (f) of each side for SrF_2:9%Eu^{3+}, x%Tb^{3+}@SiO_2 YSNFs

The diameter distribution histograms of the samples are shown in Figure S3, and the results show that the diameters of all samples conform to a normal distribution. The average diameter of each side of {PVP/[$Sr(CH_3COO)_2$+$Eu(NO_3)_3$+TEOS]}//{PVP/[$Sr(CH_3COO)_2$+$Tb(NO_3)_3$+TEOS]} JCNFs is 720.01±10.42 nm, as shown in Figure S3a. The average shell diameter of each side of [SrF_2:9%Eu^{3+}@SiO_2]//[SrF_2:7%Tb^{3+}@SiO_2] JYSNFs is 337.75±1.60 nm (Figure S3b), and the average yolk diameter of one side of [SrF_2:9%Eu^{3+}@SiO_2]//[SrF_2:7%Tb^{3+}@SiO_2] JYSNFs is 198.75±1.35 nm (Figure S3c). In addition, the average diameter of PVP/[$Sr(CH_3COO)_2$+$Eu(NO_3)_3$+$Tb(NO_3)_3$+TEOS] CNFs is 595.50 ± 1.82 nm (Figure S3d). The average shell diameter of SrF_2:9%Eu^{3+}, 7%Tb^{3+}@SiO_2 YSNFs is 350.11±1.27 nm (Figure S3e), while the average yolk diameter is 200.22 ± 1.40 nm (Figure S3f).

Figure S4 shows the elemental compositions and contents of the samples. C, N, O, Si, Pt, Eu, Tb and Sr are the main elements in the JCNFs and CNFs, which conform to the compositions of the JCNFs and CNFs (Figure S4a and S4c). After high-temperature fluorination, the N element is disappeared and the F element is appeared in [SrF_2:9%Eu^{3+}@SiO_2]//[SrF_2:7%Tb^{3+}@SiO_2] Janus yolk-shell nanofibers (Figure S4b) and SrF_2:9%Eu^{3+}, 7%Tb^{3+}@SiO_2 YSNFs (Figure S4d). The contents of C are reduced due to the decomposition and volatilization of PVP template agent at high-temperature, and the remaining peak of C comes from the conductive adhesive used in the SEM test. The presence of F element proves that F ion has been successfully introduced into the sample during the fluorination calcination process. The presence of Eu and Tb elements proves that they have been successfully doped into SrF_2 hosts. No other impurity elements are detected in the above samples, meaning that high-purity samples are obtained.

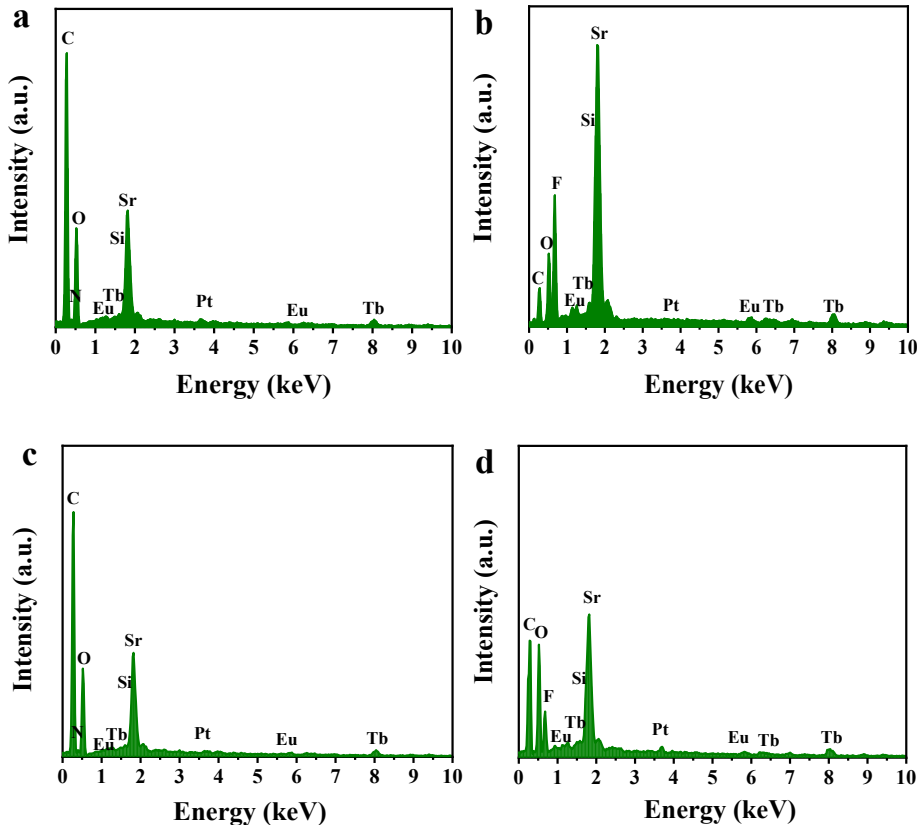

Figure S4 EDS spectra of {PVP/[$Sr(CH_3COO)_2$+$Eu(NO_3)_3$+TEOS]}//{PVP/[$Sr(CH_3COO)_2$+$Tb(NO_3)_3$+TEOS]} JCNFs (a), [SrF_2:9%Eu^{3+}@SiO_2]//[SrF_2:7%Tb^{3+}@SiO_2] JYSNFs (b), PVP/[$Sr(CH_3COO)_2$+$Eu(NO_3)_3$+$Tb(NO_3)_3$+TEOS] CNFs (c) and SrF_2:9%Eu^{3+}, x%Tb^{3+}@SiO_2 YSNFs (d)

The SEM images of PVP/[$Sr(CH_3COO)_2$+$Eu(NO_3)_3$] composite nanofibers (the diameter is 514.61±9.17 nm, Figure S6a), PVP/[$Sr(CH_3COO)_2$+$Tb(NO_3)_3$] composite nanofibers (the diameter is 590.65±7.64 nm, Figure S6b) and PVP/[$Sr(CH_3COO)_2$+$Eu(NO_3)_3$+$Tb(NO_3)_3$] composite nanofibers (the diameter is 525.69±6.93 nm, Figure

S6c) are given in Figure S5a, S5b and S5c, respectively. Additionally, the SEM micrographs of SrF_2:9%Eu^{3+} nanofibers (the diameter is 402.13±8.07 nm, Figure S6d), SrF_2:7%Tb^{3+} nanofibers (the diameter is 436.05±3.01 nm, Figure S6e) and SrF_2:9%Eu^{3+}, 7%Tb^{3+} nanofibers (the diameter is 433.11±4.91 nm, Figure S6f) are respectively given in Figure S5d, S5e and S5f. The composite nanofibers have smooth and good dispersion, and after calcination, the surface of the inorganic nanofibers becomes rough.

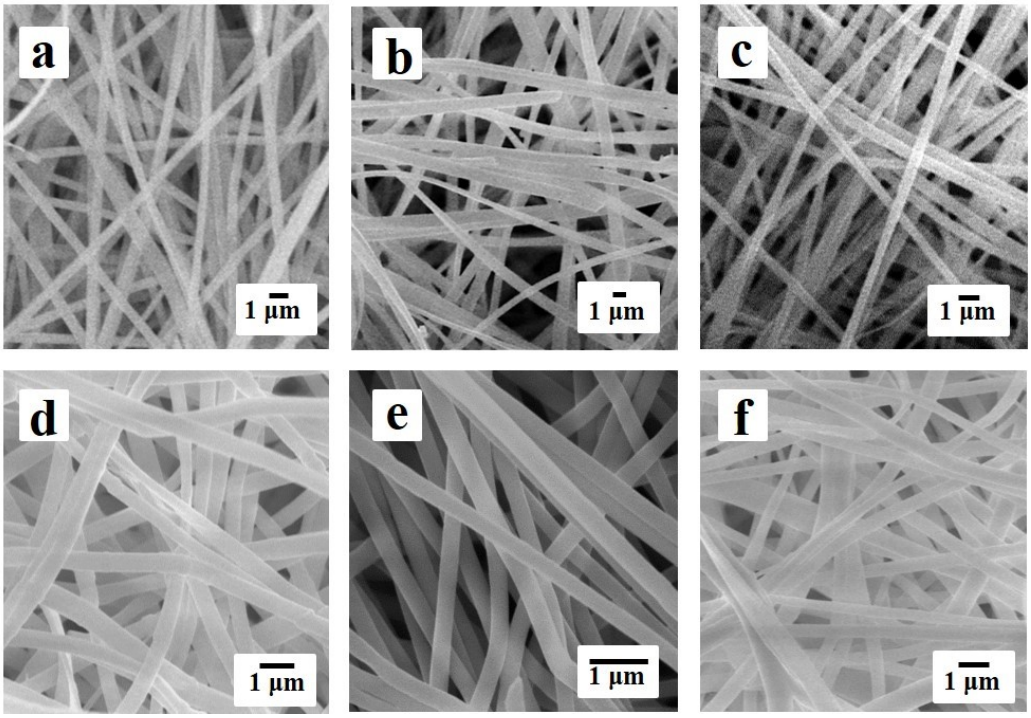

Figure S5 SEM micrographs of PVP/[$Sr(CH_3COO)_2$+$Eu(NO_3)_3$] composite nanofibers (a), PVP/[$Sr(CH_3COO)_2$+$Tb(NO_3)_3$] composite nanofibers (b), PVP/[$Sr(CH_3COO)_2$+$Eu(NO_3)_3$+$Tb(NO_3)_3$] composite nanofibers (c), SrF_2:9%Eu^{3+} nanofibers (d), SrF_2:7%Tb^{3+} nanofibers (e) and SrF_2:9%Eu^{3+}, 7%Tb^{3+} nanofibers (f)

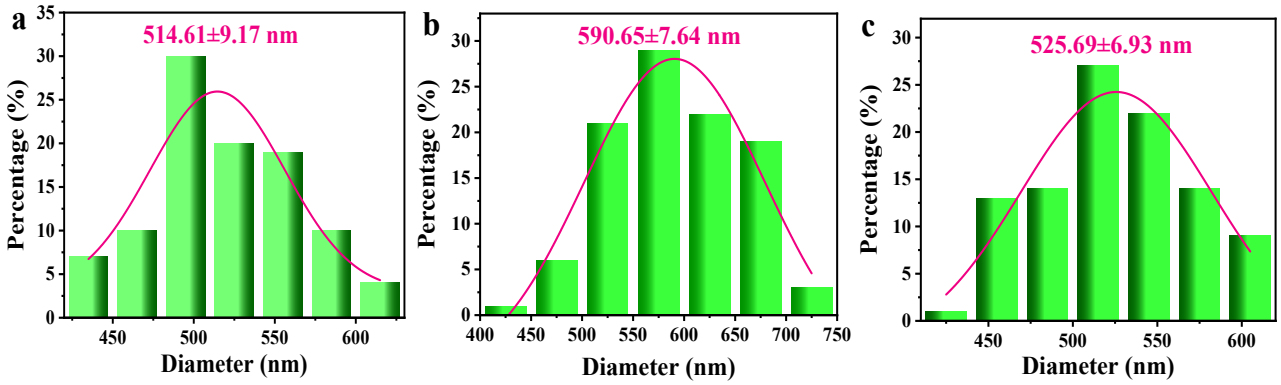

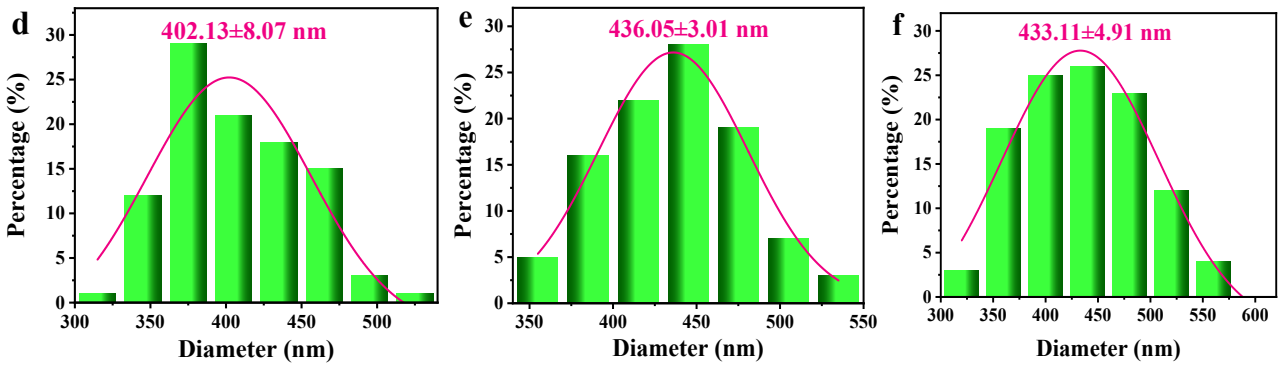

Figure S6 Histograms of diameters distribution of PVP/[$Sr(CH_3COO)_2$+$Eu(NO_3)_3$] composite nanofibers (a), PVP/[$Sr(CH_3COO)_2$+$Tb(NO_3)_3$] composite nanofibers (b), PVP/[$Sr(CH_3COO)_2$+$Eu(NO_3)_3$+$Tb(NO_3)_3$] composite nanofibers (c), SrF_2:9%Eu^{3+} nanofibers (d), SrF_2:7%Tb^{3+} nanofibers (e) and SrF_2:9%Eu^{3+}, 7%Tb^{3+} nanofibers (f)

Figure 4a shows the emission (λ_{ex}=252 nm) and excitation (λ_{em}=545 nm) spectra of the SrF_2:7%Tb^{3+} nanofibers. At the monitoring wavelength of 545 nm, the excitation peaks of SrF_2:7%Tb^{3+} nanofibers at 252 and 264 nm are assigned to the 4f→4f5d, and the excitation peak of SrF_2:7%Tb^{3+} nanofibers at 282 nm is attributed to 4f→4f transition of Tb^{3+} ion, respectively. There are also several excitation peaks at 302, 314, 340, 352, 368 and 374 nm, which are attributed to the $^7F_6$→$^5H_6$, $^7F_6$→$^5D_0$, $^7F_6$→$^5L_8$, $^7F_6$→$^5G_4$, $^7F_6$→$^5G_5$ and $^7F_6$→$^5D_3$ transition of the Tb^{3+} ions [S1], respectively. Under the 252-nm UV light excitation, some emission peaks of Tb^{3+} ion at 452 ($^5D_3$→$^7F_3$), 467 ($^5D_3$→$^7F_2$), 490 ($^5D_4$→$^7F_6$), 545 ($^5D_4$→$^7F_5$), 585 ($^5D_4$→$^7F_4$) and 622 ($^5D_4$→$^7F_3$) nm could be found [S2]. In addition, the emission (λ_{ex}=393 nm) and excitation (λ_{em}=592 nm) spectra of the SrF_2:9%Eu^{3+} nanofibers are provided in Figure 4b. Under the monitoring wavelength of 592 nm, the excitation peak at 285 nm comes from the 4f→4f5d transition of the Eu^{3+} ion, and several excitation peaks at 297, 318, 361, 381 and 393 nm are observed and ascribed to the $^7F_0$→$^5F_2$, $^7F_0$→$^5H_6$, $^7F_0$→$^5D_4$, $^7F_0$→$^5G_2$ and $^7F_0$→$^5L_6$ of Eu^{3+} ions [S3], respectively. At 393-nm UV light excitation, the energy levels transitions from $^5D_0$ to ^7F_J (J=1 and 2) states of Eu^{3+} ions generate emission peaks at 592 and 616 nm [S4], respectively.

Figure S7 exhibits the energy levels transition mechanism of Tb^{3+} and Eu^{3+} in SrF_2 nanofibers. Under 252-nm UV light excitation, the Tb^{3+} ion in the $^7F_6$ ground state are stimulated to $^5D_2$ excited state, then the Tb^{3+} ion in the $^5D_2$ excited state relaxes to the $^5D_3$ states and $^5D_4$ states of Tb^{3+} ion, and the return to the ^7F_J (J=0-6) states, resulting in green-light emission. The $^5D_4$ state of Tb^{3+} ion is energetically close to the $^5D_1$ state of Eu^{3+} ion, and transfers the absorbed energy to the surrounding Eu^{3+} along the energy transfer (ET) path, promoting the Eu^{3+} ion from the $^7F_0$ ground state to the $^5D_1$ state. The Eu^{3+} in the $^5D_1$ state can first relax to the $^5D_0$ state, and then transit to the ^7F_J (J=0-6) ground state of Eu^{3+} ion, producing red-light emission [S1, S2].

Further, color purities of the specimens are calculated by using the following formula [S5]:

$$Color\ purity = \frac{\sqrt{(x-x_i)^2+(y-y_i)^2}}{\sqrt{(x_d-x_i)^2+(y_d-y_i)^2}} \times 100\%$$

Here, (x, y), (x_i, y_i) and (x_d, y_d) represent the CIE coordinate of the specimens, the CIE coordinate of white illuminant point and the CIE coordinate of dominant wavelength in the emission, respectively. The CIE coordinate (x, y) and color purity values of the [SrF_2:9%Eu^{3+}@SiO_2]//[SrF_2:x%Tb^{3+}@SiO_2] JYSNFs SrF_2:9%Eu^{3+}, x%Tb^{3+}@SiO_2 YSNFs under different excitation wavelengths are given in Table S4.

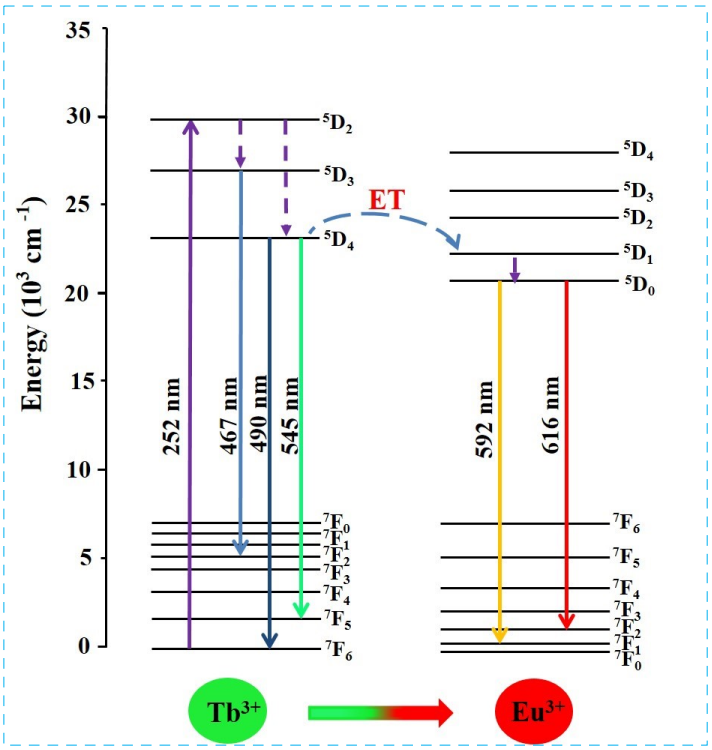

Figure S7 Simplified energy level scheme of ET processes of Tb^{3+}→Eu^{3+}

Table S4 CIE coordinate (x, y) and color purity of the [SrF_2:9%Eu^{3+}@SiO_2]//[SrF_2:x%Tb^{3+}@SiO_2] JYSNFs SrF_2:9%Eu^{3+}, x%Tb^{3+}@SiO_2 YSNFs under different excitation wavelengths

Specimens	Excitation wavelengths	CIE (x, y)	Color purity (%)
[SrF_2:9%Eu^{3+}@SiO_2]//[SrF_2:1%Tb^{3+}@SiO_2] JYSNFs	λ_{ex}=252 nm	(0.3437, 0.2978)	14.1
[SrF_2:9%Eu^{3+}@SiO_2]//[SrF_2:3%Tb^{3+}@SiO_2] JYSNFs	λ_{ex}=252 nm	(0.3301, 0.3285)	1.7
[SrF_2:9%Eu^{3+}@SiO_2]//[SrF_2:5%Tb^{3+}@SiO_2] JYSNFs	λ_{ex}=252 nm	(0.3022, 0.3861)	15.5
[SrF_2:9%Eu^{3+}@SiO_2]//[SrF_2:7%Tb^{3+}@SiO_2] JYSNFs	λ_{ex}=252 nm	(0.3032, 0.3951)	17.4
[SrF_2:9%Eu^{3+}@SiO_2]//[SrF_2:9%Tb^{3+}@SiO_2] JYSNFs	λ_{ex}=252 nm	(0.3016, 0.4158)	15.7
[SrF_2:9%Eu^{3+}@SiO_2]//[SrF_2:1%Tb^{3+}@SiO_2]	λ_{ex}=393 nm	(0.5362, 0.3967)	81.3

JYSNFs			
$[SrF_2:9\%Eu^{3+}@SiO_2]//[SrF_2:3\%Tb^{3+}@SiO_2]$ JYSNFs	λ_{ex}=393 nm	(0.5232, 0.4020)	77.1
$[SrF_2:9\%Eu^{3+}@SiO_2]//[SrF_2:5\%Tb^{3+}@SiO_2]$ JYSNFs	λ_{ex}=393 nm	(0.4869, 0.3865)	62.1
$[SrF_2:9\%Eu^{3+}@SiO_2]//[SrF_2:7\%Tb^{3+}@SiO_2]$ JYSNFs	λ_{ex}=393 nm	(0.5032, 0.3924)	68.6
$[SrF_2:9\%Eu^{3+}@SiO_2]//[SrF_2:9\%Tb^{3+}@SiO_2]$ JYSNFs	λ_{ex}=393 nm	(0.4831, 0.3848)	60.4
SrF_2:9%Eu^{3+}, 1%Tb^{3+}@SiO_2 YSNFs	λ_{ex}=252 nm	(0.4211, 0.4927)	69.9
SrF_2:9%Eu^{3+}, 3%Tb^{3+}@SiO_2 YSNFs	λ_{ex}=252 nm	(0.4222, 0.4614)	59.7
SrF_2:9%Eu^{3+}, 5%Tb^{3+}@SiO_2 YSNFs	λ_{ex}=252 nm	(0.4277, 0.4588)	60.3
SrF_2:9%Eu^{3+}, 7%Tb^{3+}@SiO_2 YSNFs	λ_{ex}=252 nm	(0.4276, 0.4679)	63.1
SrF_2:9%Eu^{3+}, 9%Tb^{3+}@SiO_2 YSNFs	λ_{ex}=252 nm	(0.3668, 0.4767)	36.9
SrF_2:9%Eu^{3+}, 1%Tb^{3+}@SiO_2 YSNFs	λ_{ex}=393 nm	(0.5445, 0.3862)	83.3
SrF_2:9%Eu^{3+}, 3%Tb^{3+}@SiO_2 YSNFs	λ_{ex}=393 nm	(0.5399, 0.4007)	83.1
SrF_2:9%Eu^{3+}, 5%Tb^{3+}@SiO_2 YSNFs	λ_{ex}=393 nm	(0.5119, 0.3826)	70.7
SrF_2:9%Eu^{3+}, 7%Tb^{3+}@SiO_2 YSNFs	λ_{ex}=393 nm	(0.5646, 0.4068)	92.8
SrF_2:9%Eu^{3+}, 9%Tb^{3+}@SiO_2 YSNFs	λ_{ex}=393 nm	(0.5144, 0.3909)	72.6

References

[S1] N. Guo, Y. Pan, W. Z. Lv, R. Z. Ouyang, B. Q. Shao, Optical thermometric properties in Tb^{3+} and Eu^{3+}-coactivated dual-emissive fluorophosphate phosphors, *Opt. Laser. Technol.,* 2020, **123**, 105938.

[S2] H. Guo, L. M. Teng, R. F. Wei, Tunable white light and energy transfer of Eu^{2+}-Tb^{3+}-Eu^{3+} tri-activated glasses synthesized in air, *J. Am. Ceram. Soc.,* 2019, **12**, 6777-6786.

[S3] W. T. Ding, Y. Zhang, B. Wang, W. F. Zhu and R. Zhang, Structure, luminescence and energy transfer of $Eu^{2,3+}$/Tb^{3+} co-doped transparent glass ceramics containing a-$Ca_3(PO_4)_2$ nanocrystals, *J. Alloys. Compd.*, 2020, **815,** 152661.

[S4] A. I. Becerro, M. Allix, M. Laguna, D. G. Mancebo, C. Genevois, A. Caballero, G. Lozano, N. O. Nunez and M. Ocana, Revealing the substitution mechanism in Eu^{3+}:$CaMoO_4$ and Eu^{3+},Na^{+}:$CaMoO_4$ phosphors, *J. Mater. Chem. C*, 2018**, 6,** 12830-12840.

[S5] D. A. Hakeem, J. W. Pi, S. W. Kim, K. Park, New $Y_2LuCaAl_2SiO_{12}$:Ln (Ln = Ce^{3+}, Eu^{3+}, and Tb^{3+}) phosphors for white LED applications, *Inorg. Chem. Front.,* 2018, **5,** 1336-1345.